Electrical Power and Energy Systems 147 (2023) 108903

Contents lists available at ScienceDirect

International Journal of Electrical Power and Energy Systems

journal homepage: www.elsevier.com/locate/ijepes

Single-ended limiting inductor voltage-ratio-derivative protection scheme for VSC-HVDC grids

María José Pérez-Molina *, Pablo Eguia, D. Marene Larruskain, Esther Torres, Oihane Abarrategi, Juan C. Sarmiento-Vintimilla

Department of Electrical Engineering, University of the Basque Country UPV/EHU, Plaza Ingeniero Torres Quevedo, 1, Bilbao, Spain

ARTICLE INFO

Keywords:
HVDC
Limiting inductor
Protection system
Single-ended
Voltage-ratio-derivative

ABSTRACT

Single-ended protection systems present the characteristics needed to fulfil the restrictive speed requirement related to high voltage direct current grids. This paper proposes a novel single-ended protection algorithm based on the DC voltage across the limiting inductors placed at each link end. Voltage measurements are taken at both terminals of the limiting inductors. The ratio between the link- and bus-side voltages enables fault discrimination between forward and backward fault conditions while providing directionality. Moreover, the derivative of the voltage-ratio is calculated in order to enable fast fault detection. The combined operation of these two algorithms avoids nuisance operations against fluctuations and close-up external faults. A trip signal is only issued to the circuit breakers when the individual criteria of both algorithms are simultaneously fulfilled. According to this, a protection scheme is developed, which covers link primary and backup as well as busbar protections. The performance of the proposed protection scheme is evaluated through simulations in a four-terminal grid. The selective, sensitive and accurate performance of the proposed protection scheme is demonstrated against faults up to 250 Ω while employing only local measurements, common limiting inductor sizes and a relatively low sampling frequency. Thus, the proposed protection scheme overcomes the sensitivity limitations related to high-resistance fault detection presented in derivative-based algorithms. Its proper operation under noise disturbances is also demonstrated.

1. Introduction

The protection system of a High Voltage Direct Current (HVDC) grid is vital due to the requirement of speed imposed by the Direct Current (DC) fault characteristics and the overcurrent withstand capability of the power electronic components that compose a Voltage Source Converter (VSC) [1]. Thus, the fault detection, location and clearance must be achieved in a very short range of time [2]. Hence, fast protection algorithms are needed besides fast HVDC Circuit Breakers (CB) [3], such as hybrid CBs [4].

Single-ended algorithms present an advantage of speed against double-ended algorithms, since the performance of the latter algorithms is restricted by the time delay imposed by their own communication system [5]. Therefore, this paper deals with single-ended algorithms, which are more appropriate for large Multi-Terminal (MT) HVDC grids with long transmission distances, in order to meet the critical requirement of speed [6].

Researchers have addressed single-ended protection algorithms over the last years. The most common algorithms monitor the magnitude of the measured signal and compare it to a pre-set threshold value. Thus, the fault-induced signal variations can be detected. The overcurrent algorithm, which measures the DC current magnitude [7], has been widely researched in the literature [8]. Similarly, the undervoltage algorithm measures the DC voltage magnitude [9], detecting the characteristic voltage drop related to a fault condition [10].

Likewise, other single-ended algorithms mathematically process the signal measurements by, e.g., calculating their derivative and, then, comparing it with a pre-selected threshold value [11]. Hence, they are based on detecting the fault-induced variations on the rate of change of the measurement's magnitude [12]. Due to this, the derivative-based algorithms present great relevance since they can achieve faster fault detection. Some of the most usual derivative-based algorithms are the rate-of-change-of-current (ROCOC) [13] and the rate-of-change-of-voltage (ROCOV) [14]. Other single-ended algorithms are based on

* Corresponding author.
E-mail address: mariajose.perez@ehu.eus (M.J. Pérez-Molina).

https://doi.org/10.1016/j.ijepes.2022.108903
Received 8 July 2022; Received in revised form 24 October 2022; Accepted 15 December 2022
Available online 22 December 2022

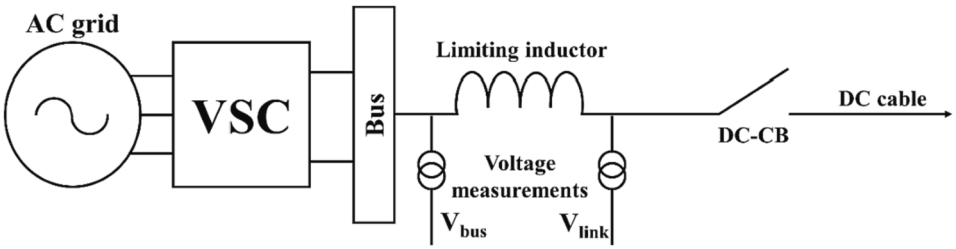

Fig. 1. Voltage measurement diagram.

processing the travelling wave characteristics. The frequency spectrum of the traveling wave can be extracted using Wavelet transforms and fault discrimination can be achieved according to its frequency content [15]. Artificial-intelligence-based algorithms employing artificial neural networks can also be single-ended algorithms [16].

Since the used measurements are locally taken, single-ended algorithms present a fast performance [17]. However, they are challenging in selectivity terms which can be enhanced by using limiting inductors and a suitable threshold value [18]. The threshold value must be selected depending on the system and protection algorithm characteristics. A higher value will ensure the detection of only fault conditions located inside the protection zone, i.e., an improved selectivity [19]. However, a very high value may adversely affect the algorithm's sensitivity. This way, some internal fault conditions may not be detected.

On the other hand, limiting inductors are commonly applied to delimit the protection zones in VSC-based HVDC systems [20]. Similarly, the inductor size affects the algorithm's selectivity and sensitivity as the threshold value does. Moreover, they can reduce the rate of rise of the fault current [21]. Conversely, a large inductor size may affect the stability of the system [22].

Furthermore, the damping characteristic of the limiting inductors can be useful for fault detection purposes. The voltage across these inductors can be selected as the fault marker. During normal operation,

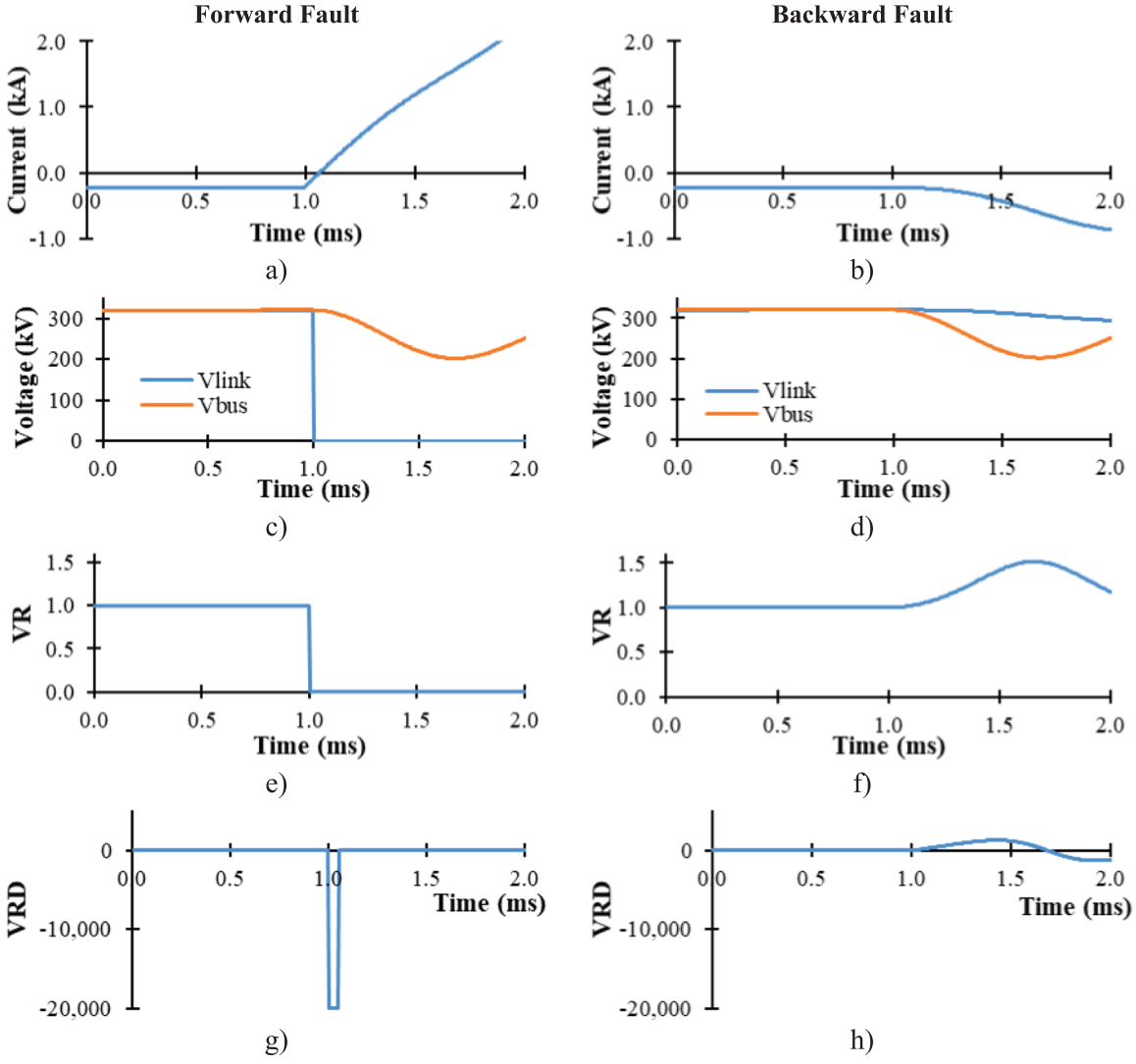

Fig. 2. Current, V_{link}, V_{bus}, VR and VRD measurements for a), c), e), g) a forward fault and b), d), f), h) a backward fault.

the voltage across the inductor is zero, since the voltage measured at both sides of the inductor is the same. However, after fault inception on the protection zone, the link-side voltage collapses sharply while the bus-side voltage drop is attenuated. Therefore, the voltage across the limiting inductor increases, making it a good indicator of the existence of a fault condition in the system. There are several algorithms in the literature which employ this feature. Reference [23] employs the voltage across the limiting inductor as a fault marker, however it presents some limitations in terms of sensitivity to high-resistance faults (up to 50 Ω) in a cable-based system. Similarly, authors of [24] present a protection system based on monitoring the voltage across the limiting inductor for an overhead line-based (OHL) grid with 150 mH limiting inductors. Reference [25] is based on calculating the ratio of the ROCOV at both sides of the limiting inductor; it presents a sensitivity limited to 50 Ω in a cable-based system and it employs a relatively high inductor size (150 mH) and a relatively high sampling frequency of 32 kHz. Moreover, it needs a undervoltage-based supervision element and it uses a communication system for improved performance. Additionally, the same authors present the same protection system in [26] but with a sampling frequency of 25 kHz. Paper [27] also employs the voltage across the limiting inductors, which present a relatively high size of 200 mH. Similarly, it does not take into account pole-to-ground faults which are more common than pole-to-pole faults and which are more challenging to detect under large fault resistances due to attenuation [28]. Moreover, any of these references do not analyse the influence of the noise disturbance on the algorithms' operation which is of great relevance.

In this sense, this paper presents a novel single-ended protection algorithm based on the voltage-ratio between the measurements taken at both sides of the limiting inductor, which is able to overcome the limitations presented in the state of art, i.e., low sensitivity to high-resistance faults [29]; and high sampling frequencies and inductor sizes. The sign of the voltage-ratio provides discrimination between forward and backward faults and, thus, a directional element to the protection system, while its derivative is calculated to allow fault detection with high speed. Taking into account its characteristics, a protection scheme is developed. Link primary and backup protections are covered, as well as busbar protection. The protection scheme employs relatively low sampling frequencies and inductor sizes. Moreover, it presents a sensitive and fast operation against high-resistance fault conditions up to 250 Ω, without employing a communication system, and, thus, it overcomes the sensitivity limitations related to high-resistance fault detection which are present in common single-ended derivative-based algorithms. Besides, there is no need of supervision elements for its proper operation while its correct performance under noise disturbances is demonstrated.

The remainder of the present work is arranged as follows: Section 2 explains thoroughly the proposed protection scheme. Section 3, firstly, introduces the four-terminal model grid used in the simulations. Then, the proposed algorithm is evaluated against different fault conditions. Afterwards, the influence of noise disturbance in its operation is assessed and its performance is compared with similar inductor-voltage-based algorithms. Finally, the conclusions of the presented work are detailed in Section 4.

2. Limiting inductor voltage-ratio-derivative protection scheme

Using limiting inductors allows a clear delimitation of the algorithm's protection zone since external traveling waves are affected by their damping characteristic. The proposed protection algorithm is based on the voltage difference between both sides of the limiting inductors located in the transmission links (1). This way, the voltage is measured at both sides of the limiting inductor as shown in Fig. 1.

$$V_L = L \cdot \frac{di}{dt} = V_{bus} - V_{link} \tag{1}$$

where V_L is the voltage across the inductor, L is the inductor size, di/dt is the current-derivative and V_{bus} and V_{link} are the voltage measurements taken at the bus- and link-side of the inductor, respectively.

2.1. Voltage-ratio algorithm

The two voltage measurements V_{link} and V_{bus} are equal during normal operation, since the DC current is constant, as it is shown in (2).

$$\text{Normal Operation}: i_{DC} = \text{constant} \Rightarrow \frac{di}{dt} = \frac{(V_{bus} - V_{link})}{L} = 0 \Leftrightarrow V_{bus} = V_{link} \tag{2}$$

Meanwhile, a voltage difference is produced after fault inception and the rate of increase of the DC current presents a high positive value (Fig. 2-a; fault inception at t = 1 ms). This way, when a forward fault occurs the voltage measurement at the link-side of the limiting inductor V_{link} presents a lower value than the voltage measurement at the bus-side V_{bus} (3), as it can be seen in Fig. 2-c.

$$\text{Forward Fault}: i_{DC} > 0 \Rightarrow \frac{di}{dt} = \frac{(V_{bus} - V_{link})}{L} > 0 \Leftrightarrow V_{bus} > V_{link} \tag{3}$$

On the other hand, when a backward fault takes place, V_{link} presents a value higher than V_{bus} since the DC current inverts its direction and flows out of the protection zone (4) (Fig. 2-b and -d).

$$\text{Backward Fault}: i_{DC} < 0 \Rightarrow \frac{di}{dt} = \frac{(V_{bus} - V_{link})}{L} < 0 \Leftrightarrow V_{bus} < V_{link} \tag{4}$$

Thus, the voltage-ratio (VR) can be employed as a fault marker (5).

$$VR = \frac{V_{link}}{V_{bus}} \tag{5}$$

During normal operation, since both voltage measurements are equal, the VR is equal to one (6).

$$\text{Normal Operation}: V_{bus} = V_{link} \Rightarrow VR = 1 \tag{6}$$

However, the VR presents a value lower than one during forward fault conditions since V_{link} is lower than V_{bus} (7), as it can be seen in Fig. 2-e.

$$\text{Forward Fault}: V_{bus} > V_{link} \Rightarrow VR < 1 \tag{7}$$

Otherwise, Fig. 2-f shows how the VR presents a value higher than one during backward fault conditions (8).

$$\text{Backward Fault}: V_{bus} < V_{link} \Rightarrow VR > 1 \tag{8}$$

Therefore, the VR provides directionality to the protection scheme by comparing the VR with pre-selected threshold values: THR_1 for forward faults (9) and THR_2 for backward faults (10). THR_1 takes a value between zero and one and THR_2 is a value higher than 1.

$$\text{Forward Fault}: VR < THR_1 \tag{9}$$

$$\text{Backward Fault}: VR > THR_2 \tag{10}$$

2.2. Voltage-ratio-derivative algorithm

Derivative-based algorithms present a fast fault detection capability, then, the derivative of the VR, i.e., the voltage-ratio-derivative (VRD), is calculated as in (11), where VR_{t_1} is the VR value calculated at time t_1 and VR_{t_2} is the VR value calculated at time t_2, being t_2 higher than t_1.

$$VRD = \frac{dVR}{dt} = \frac{VR_{t_2} - VR_{t_1}}{t_2 - t_1} \tag{11}$$

During normal operation, the VRD is equal to zero since the VR is constant and equal to one, as it is shown in (6) and (12).

$$\text{Normal Operation}: VR = 1 \Rightarrow VRD = 0 \tag{12}$$

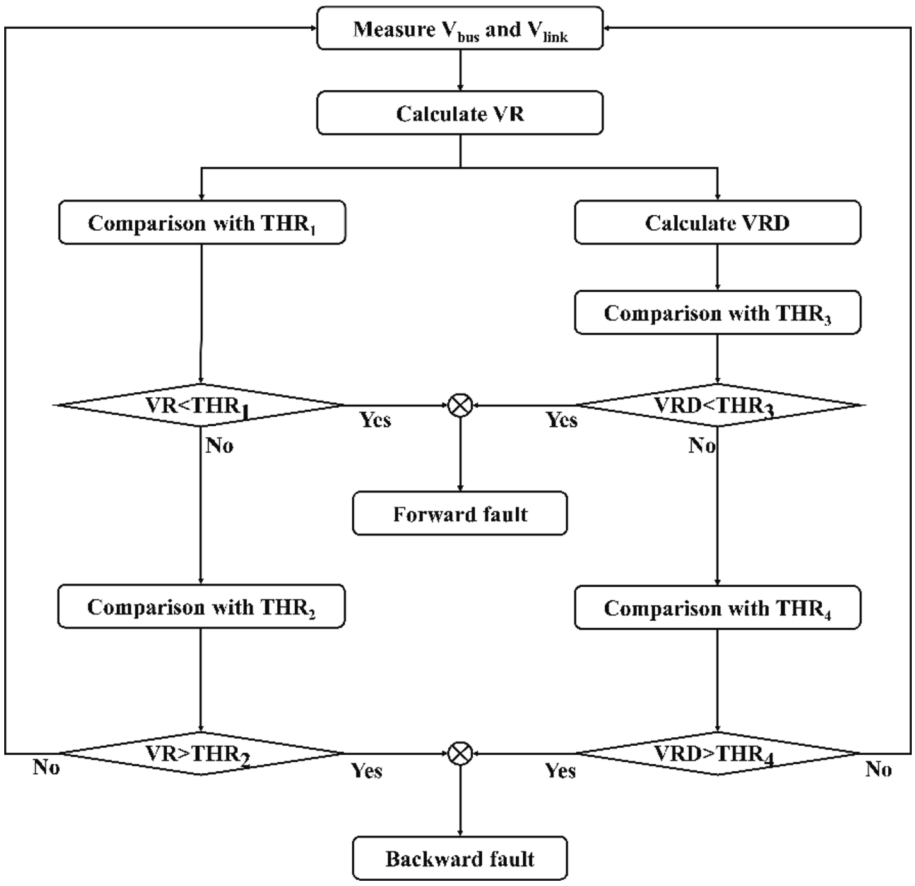

Fig. 3. Flow chart of the LIVRD protection scheme.

According to (7), the VR drops to a value lower than one during a forward fault, hence, making the VRD drop to a negative value (13), as it is depicted in Fig. 2-g.

$$\text{Forward Fault}: \ VR < 1 \Rightarrow VRD < 0 \tag{13}$$

Meanwhile, the VRD presents a positive value (14) since the VR increases over one during a backward fault, as stated in (8) and depicted in Fig. 2-h.

$$\text{Backward Fault}: \ VR > 1 \Rightarrow VRD > 0 \tag{14}$$

Moreover, the VRD is compared to threshold values THR_3 for forward fault detection (15) and THR_4 for backward fault detection (16). THR_3 takes a negative value while THR_4 is a positive value.

$$\text{Forward Fault}: \ VRD < THR_3 \tag{15}$$

$$\text{Backward Fault}: \ VRD > THR_4 \tag{16}$$

2.3. Protection scheme

The VR and VRD algorithms are combined into the Limiting Inductor Voltage-Ratio-Derivative-based (LIVRD) protection scheme. This combination improves the selectivity of the protection scheme without significantly affecting the operation speed. The combined performance of these two algorithms when their individual criteria are fulfilled avoids nuisance operation due to transients induced by non-fault conditions.

The VRD algorithm presents very fast fault detection by itself. However, it might present nuisance operations since some fluctuations on the measured signals due to normal operation of the system could produce a negative VRD. Thus, in case the condition stated in criterion (15) is achieved, a possible forward fault condition is detected but no trip signal is sent to the circuit breaker until the VR condition of criterion (9) is also fulfilled. Therefore, forward fault detection is achieved when criteria (9) and (15) are fulfilled simultaneously, as it is depicted in (17). Similarly, backward fault detection is achieved when criteria (10) and (16) are satisfied, as it is shown in (18).

$$\text{Forward Fault Detection}: \begin{cases} VR < THR_1 \\ VRD < THR_3 \end{cases} \tag{17}$$

$$\text{Backward Fault Detection}: \begin{cases} VR > THR_2 \\ VRD > THR_4 \end{cases} \tag{18}$$

Fig. 3 shows the flow chart of the proposed LIVRD protection scheme.

The proposed LIVRD based protection scheme includes link primary and backup as well as busbar protection.

2.3.1. Link primary protection

Link protection covers the protection of each link of the system as an independent element. Hence, limiting inductors are required at the ends of each link in order to properly delimit the protection zones. This way, only the protected link is isolated when a fault occurs within it.

Link primary protection is related to the detection of all faults occurring inside the corresponding protection zone, i.e., forward fault detection. Thus, an internal fault to the protection zone is detected by the primary protection when criterion (17) is fulfilled. Meanwhile, if a backward fault is detected primary protection is blocked, preventing nuisance operation due to transients, e.g., those induced by the opening of a CB.

2.3.2. Link backup protection

In case the link primary protection fails to detect a fault condition due to a problem in its operation, the fault will not be cleared by the

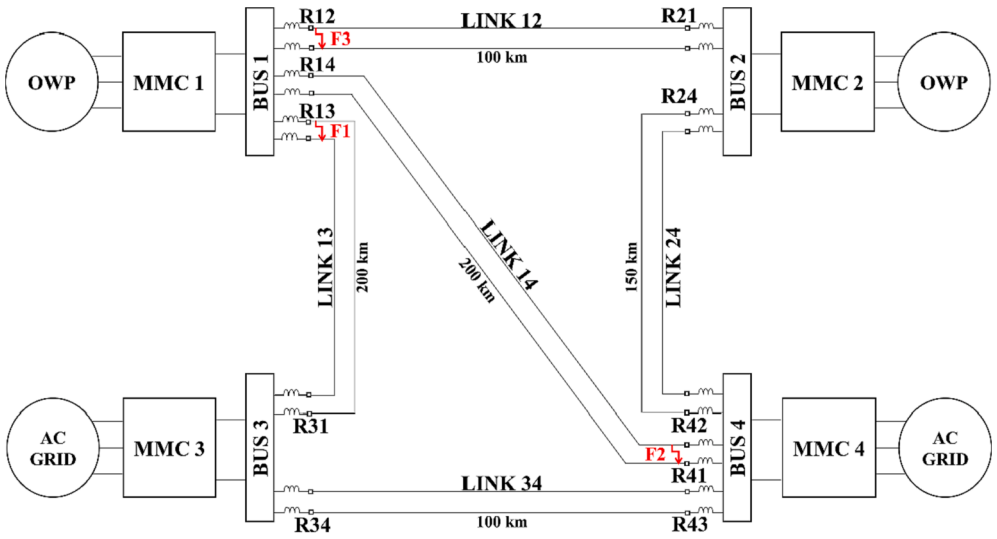

Fig. 4. Locations of the simulated fault conditions on the four-terminal grid model scheme.

corresponding circuit breakers, since they have not received the required trip signal for its operation. Therefore, a link backup protection is needed in order to allow fault detection in case of failure in the primary relay.

The backward fault detection is employed in the link backup protection, which is in charge of operating when a neighbouring relay presents a failure. Therefore, an external fault to the primary protection zone is detected by the backup protection when criterion (18) is fulfilled. Then, backup protection operates and a trip signal is sent to the corresponding circuit breaker when all relays interconnected to the same bus as the affected one detect a backward external fault, as in (19) where $R_{i,j}$ represents the relay located in link "ij" which interconnects Bus "i" and Bus "j", being Ri,j located closer to Bus "i". This way, if criterion (19) is fulfilled, the security of the protection system would be improved since no trip signal will be sent until all neighbouring relays have detected an external fault. However, the backup protection could also be individually implemented in each relay, so if one neighbouring relay, regardless of the others, detects an external fault (18), the backup protection will be initiated. The latter alternative will entail a reduced security of the protection system in comparison with the former.

$$\text{For Bus}_i \text{ and failure in } R_{i,a} \Rightarrow \forall R_{i,j} \bigwedge (j \neq a) : \begin{cases} VR_{R_{i,j}} > THR_{2_{R_{i,j}}} \\ VRD_{R_{i,j}} > THR_{4_{R_{i,j}}} \end{cases} \quad (19)$$

2.3.3. Busbar protection

Busbar protection can also be developed using the proposed LIVRD protection algorithm. A busbar fault is detected when all the relays interconnected to the affected bus detect a backward external fault, as it is shown in equation (20).

$$\text{For a fault in Bus}_i \Rightarrow \forall R_{i,j} : \begin{cases} VR_{R_{i,j}} > THR_{2_{R_{i,j}}} \\ VRD_{R_{i,j}} > THR_{4_{R_{i,j}}} \end{cases} \quad (20)$$

Thus, the developed protection scheme is based on the single-ended limiting inductor voltage-ratio-derivative algorithm proposed in this work. It not only covers the link protection, as both primary and backup protections, but also the busbar protection.

3. Study case

The proposed LIVRD protection scheme is evaluated in the four-terminal HVDC grid depicted in Fig. 4, whose features are presented in [30,31]. Half-bridge Modular Multilevel Converters (MMC) are implemented with a rated power of 900 MVA for MMCs 1, 2 and 3 and of 1200 MVA for MMC 4. Five undersea cables interconnect the terminals, being their lengths 200 km (links 13 and 14), 150 km (link 24) and 100 km (link 12 and 34).

Limiting inductors (100 mH) in series with hybrid HVDC CBs (operating time: 2 ms) are placed at the borders of each link. Then, the protection system follows a full-selective fault-clearing strategy, i.e., every link is treated as an independent protection zone. During a fault condition, only the affected protection zone is de-energized while the rest of the grid remains operative.

In the following subsections, the process of selecting adequate threshold values is firstly described. Then, the performance of the algorithm is analysed against several faults, varying its type, location and resistance. Worst fault case scenarios are simulated in order to test the performance of the proposed protection scheme algorithm, i.e., close-up solid Pole-to-Pole (PtP) faults and remote high-resistance Pole-to-Ground (PtG) faults. In addition, other fault conditions with different resistances and located at different distances in link 14 have also been simulated to evaluate the operation speed of the LIVRD protection scheme.

Fig. 4 shows the locations of the simulated fault conditions. Moreover, its performance during a busbar fault in Bus 1 is also evaluated. Following, the influence of the noise disturbance in the LIVRD protection scheme is assessed. Afterwards, the main features of the LIVRD protection scheme are evaluated in comparison with other inductor-voltage-based algorithms found in the literature.

3.1. Threshold selection process

In order to improve the selectivity and sensitivity of the LIVRD protection scheme, the thresholds defined in (9), (10), (15) and (16) have been carefully selected taking into account the worst case scenarios for each relay as well as transients induced by the opening of a neighbouring CB. A maximum fault resistance of 250 Ω is taken into account in the selection process, so the sensitivity of the protection scheme is ensured, at least, up to 250 Ω. Likewise, these worst fault cases have been analysed for both solid and 250 Ω faults and both PtP and PtG faults, even though PtP faults are not common in cable-based systems. This ensures a suitable performance of the proposed LIVRD protection scheme, since fault conditions with resistances higher than 200 Ω are rare [32]. Moreover, a sampling frequency of 20 kHz is used in the threshold selection process.

Firstly, threshold values THR_1 and THR_3, regarding the link primary protection, are selected in subsection 3.1.1. Then, selection of threshold values THR_2 and THR_4 is achieved in subsection 3.1.2. The latter threshold values are employed in the operation of the link backup

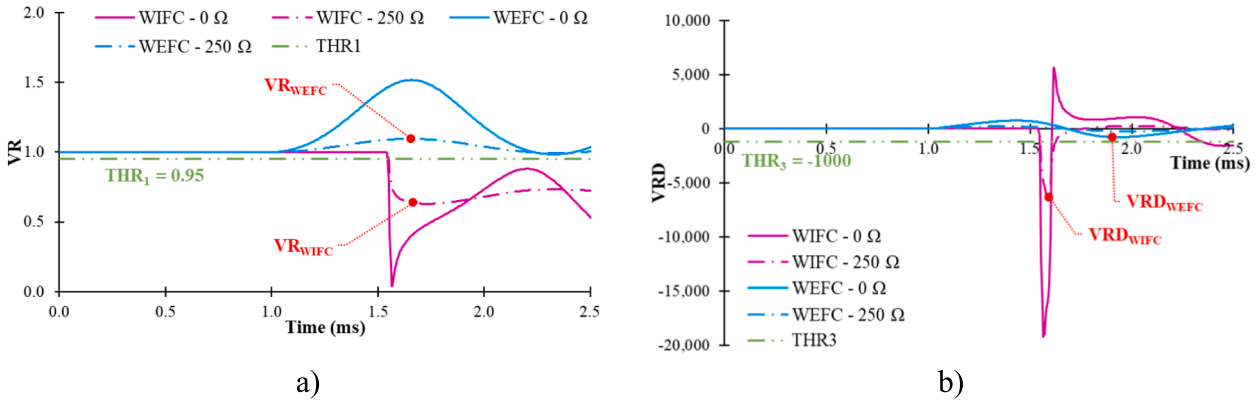

Fig. 5. Selection of threshold value a) THR_1 and b) THR_3 according to the worst fault case scenarios for relay R12.

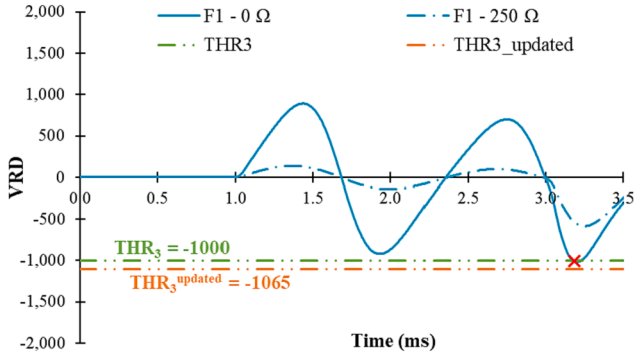

Fig. 6. Selection of the updated threshold value THR_3 for relay R12.

protection and the busbar protection.

3.1.1. Selection of link primary protection's threshold values

In the case of the link primary protection, the worst fault cases are internal faults located at the remote end of the protection zone and external faults located near the local end. Internal faults located at the remote end of the protection zone are difficult to detect due to the attenuation of the traveling wave signals. External faults located near the local end can produce a sufficiently high traveling wave to cause the false detection of an internal fault and the consequent nuisance operation. In this regard, threshold values THR_1 and THR_3 have been selected by simulating the worst fault cases for each relay, e.g., F1 is the worst internal fault case scenario for relay R31 and the worst external fault case scenario for relays R12 and R14.

According to (17), both VR and VRD values have to be lower than the link primary protection's threshold values to allow fault detection. As it was mentioned in subsections 2.1 and 2.2, THR_1 must be a value lower than one and THR_3 must be a negative value. Moreover, they must be high enough to detect the worst internal fault case and low enough to not detect external faults, including the worst external fault case. The appropriate operation of the link primary protection is ensured if the selected threshold value is a value between these critical values The selection of relay R12's threshold values is represented in Fig. 5, where pink lines represent the Worst Internal Fault Cases (WIFC), while blue lines represent the worst External Fault Cases (WEFC). Solid lines depict solid fault cases while dotdashed lines depict 250 Ω fault cases. The critical values of the worst internal and external faults cases are represented as VR_{WIFC}, VR_{WEFC}, VRD_{WIFC} and VRD_{WEFC} and are highlighted in red.

However, these critical values do not consider the transients derived from the opening of a neighbouring CB, which should not be detected by the link primary protection. Therefore, link primary protection's threshold values of 0.95 and −1000 for THR_1 and THR_3, which were initially selected, are employed in a second series of simulations taking into account the transients induced by the opening of a CB. According to the results of this second series of simulations, some initial threshold values needed to be updated since they did not ensure the proper performance of the protection system for all relays due the transients induced by the opening of a neighbouring CB. Fig. 6 shows how THR_3 of relay R12 had to be updated due the opening of relay R13 in order to clear fault F1. This way, the updated threshold values THR_1 and THR_3 for each relay that ensure a selective and accurate operation are summarized in Table 1.

Table 1
Selected threshold values for forward and backward fault detection.

Relay	Forward Fault Detection		Backward Fault Detection	
	THR_1	THR_3	THR_2	THR_4
R12	0.95	−1065	1.01	100
R13	0.95	−1000	1.01	100
R14	0.95	−1065	1.01	100
R21	0.95	−1000	1.01	100
R24	0.95	−1000	1.01	100
R31	0.95	−1000	1.01	100
R34	0.95	−1000	1.01	100
R41	0.95	−1000	1.01	100
R42	0.95	−1000	1.01	100
R43	0.95	−1000	1.01	100

Moreover, the LIVRD algorithm achieves fault detection when the VR- and VRD-based criteria are simultaneously satisfied. Thus, a time interval needs to be selected in order to verify this criterion. This way, fault detection is achieved when both criteria are fulfilled in a time interval of two consecutive samples for a 20 kHz sampling frequency, i.e., a 100 μs time interval.

It must also be highlighted that transients induced by busbar faults do not affect the selected threshold values since they present very high positive values (Fig. 14).

3.1.2. Selection of link backup/busbar protection's threshold values

Similarly, threshold values THR_2 and THR_4 regarding link backup protection and busbar protection are selected. However, the worst fault scenarios for THR_2 and THR_4 are different from the case of the link primary protection. Since the link backup protection aims to detect backward faults in the neighbouring links, the worst fault cases are a backward fault located in the remote end of the protected neighbouring link and a close-up forward fault located in the link where the relay is placed, which could produce a high enough transient triggering false backup detection.

This way, both the VR and VRD values need to be greater than the threshold value to allow backup fault detection. As it was mentioned in

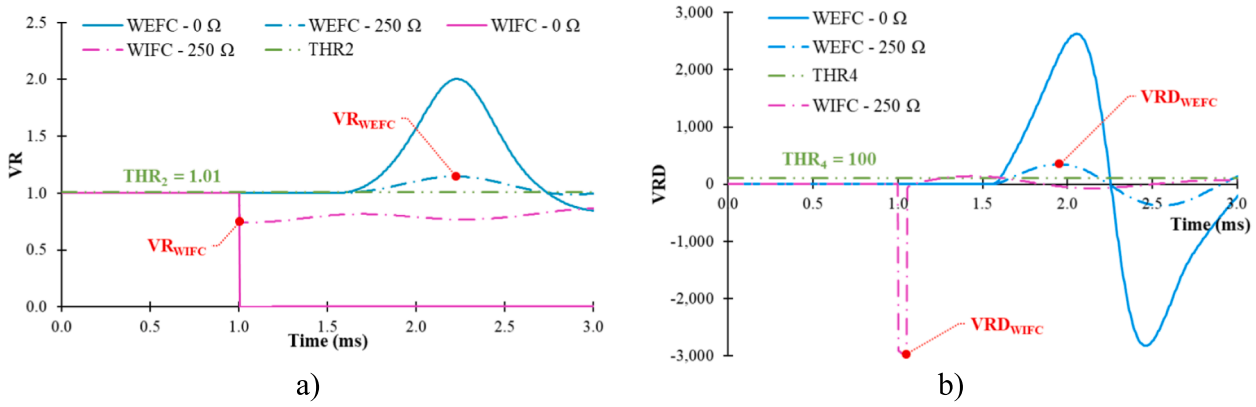

Fig. 7. Selection of threshold value THR_2 according to the worst fault case scenarios for relay R13.

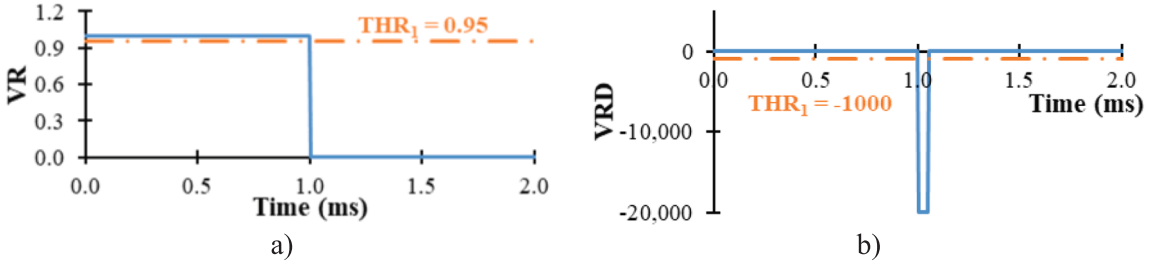

Fig. 8. a) VR and b) VRD signals measured by relay R13 for a solid PtP fault (F1) located in link 13.

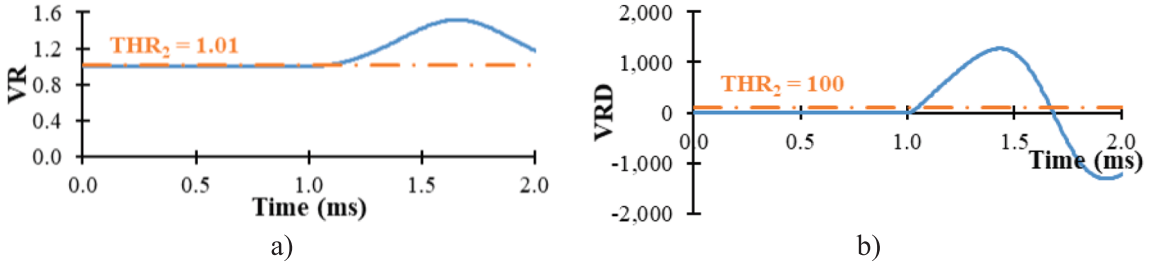

Fig. 9. a) VR and b) VRD signals measured by relay R12 for a solid PtP fault (F1) located in link 13.

subsections 2.1 and 2.2, THR_2 must be a value greater than one and THR_4 must be a positive value. Moreover, the selected threshold values must be low enough to detect the remote external fault located in the protected neighbouring link and high enough to not misdetect a close-up internal fault located in the link where the relay is placed as a backward fault. As depicted in Fig. 4, fault F1 is the worst external fault case for relay R34 whose link backup protection must be able to detect it. Conversely, fault F1 is the worst internal fault case for relay R13 and should not be misdetected as a backward fault.

Fig. 7 shows the selection process of THR_2 and THR_4 for relay R13. As in the previous case, the influence of the opening of a neighbouring CB was analysed, however, the initially selected threshold values related to link backup protection did not have to be updated. Table 1 summarizes the selected threshold values for each relay.

Similarly, a time interval of 100 μs (two consecutive samples for a sampling frequency of 20 kHz) was selected for the link backup protection in order to ensure the fulfilment of the simultaneity criterion.

The threshold values THR_2 and THR_4 and the time interval selected for the link backup protection are also appropriate for the busbar protection since busbar faults are close-up backward faults.

3.2. Performance during a close-up solid PtP fault

A close-up solid PtP fault is the worst fault case scenario in terms of maximum fault current due to the fast rate-of-rise of the fault current induced by PtP faults. According to this, a solid PtP fault (F1) located in link 13, right in front of relay R13, is simulated.

This fault case must be detected by relays R13 and R31 as a forward fault and as a backward fault by neighbouring relays R12, R14 and R34. Due to similar behaviours, only figures related to relays R12 and R13 are presented. Fig. 8 and Fig. 9 depict the VR and VRD measurements regarding relays R13 and R12, respectively.

When the solid PtP F1 fault occurs at t = 1 ms, relay R13 detects a forward fault almost instantaneously, being the link primary protection detection time (t_{Pd}) 1.050 ms, which corresponds with the first sample (for 20 kHz) after fault inception. Thus, trip signals are sent to the corresponding CBs which start the fault clearance process 2 ms after receiving the trip signal (operation time of the link primary protection, t_{Po} = 3.050 ms).

Similarly, relay R12 detects a backward fault at the detection time of the link backup protection (t_{BUd}) 1.100 ms, which is only 50 μs (one sample) after forward fault detection. Thus, backward fault detection blocks the primary protection of relay R12 preventing a nuisance

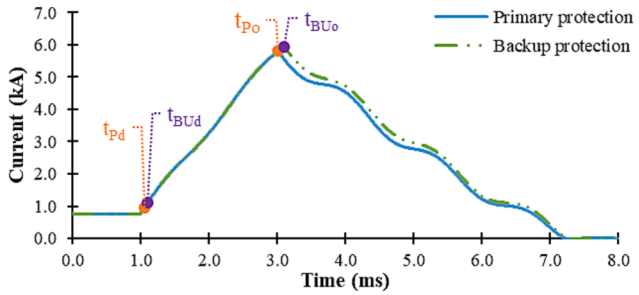

Fig. 10. Fault current measured by relay R13 for a solid PtP fault (F1) located in link 13.

operation. Moreover, if backup protection is needed due to a failure in relay R13, the operation time of the link backup protection, t_{BUo} = 3.100 ms, will not be significantly slower than the primary protection, as it can be seen in Fig. 10.

3.3. Performance during a remote high-resistance PtG fault

A remote high-resistance PtG fault is the most challenging fault case scenario in terms of fault detection, since the lower rate-of-rise of the fault current induced by PtG faults together with the attenuation produced by a high fault resistance, can make fault detection more complex. Then, a 250 Ω PtG fault (F2) located at the remote end of link 14 (from relay R14) is simulated. Its location is represented in Fig. 4.

This fault case must be detected as a forward fault and, thus, as an internal fault by relays R14 and R41. Relays R12, R13, R42 and R43 detect it as a backward fault. As in the previous subsection, only measurements regarding relays R12 and R14 are depicted in the figures. Fig. 11 and Fig. 12 present the VR and VRD signals measured by relays R14 and R12, respectively.

Fault inception occurs at t = 1 ms. Relay R14 is able to quickly detect the 250 Ω PtG F2 fault at t_{Pd} = 2.150 m, which is right after the arrival of the fault-induced traveling wave to the relay point. Thus, a trip signal is sent to the CBs which operate 2 ms after receiving it at t_{Po} = 4.150 ms. Comparing with the solid fault case, it can be seen that the VR and VRD signals (Fig. 8 and Fig. 11) are affected by the high fault resistance which causes an attenuation. However, the selected threshold values are still able to allow fault discrimination.

Similarly, relay R12 detects a backward fault at t_{BUd} = 2.400 ms, i.e., 250 μs (five samples) after forward fault detection. Thus, backward high-resistance fault detection is not greatly slower than backward solid fault detection. Moreover, if backup protection is needed due to a failure in relay R14, Fig. 13 shows that its operation (t_{BUo} = 4.400 ms) wouldn't be significantly slower than that of the primary protection.

3.4. Performance during a busbar fault

During a fault inside Bus 1 which occurs at instant t = 1 ms, the bus-side voltage V_{bus} collapses sharply to zero value (Fig. 14-a) producing very high positive values in the VR and VRD calculations according to (5) and (11) (Fig. 14-c and –d, respectively). Thus, the busbar fault is almost instantaneously detected by the busbar protection (t_{BBd}) at 1.050 ms and, then, the circuit breakers operate (busbar protection operation time t_{BBo} = 3.050 ms) to complete fault clearance, as it can be seen in Fig. 14-b, which depicts the fault currents measured by relays R12, R13 and R14. Link-side voltages V_{link} measured by all relays are superimposed in the figure as well as bus-side voltages V_{bus}. VR and VRD waves are also superimposed. Fault current presents a negative value since it is flowing from the link to the busbar.

Moreover, the event of a busbar fault does not produce the nuisance operation of any external relays. This way, the proper operation of the busbar protection is demonstrated through this analysis as well as the selective operation of the link protection.

3.5. Evaluation of the fault detection time

This subsection evaluates the operation speed of the proposed LIVRD protection scheme. Thus, the fault detection time of the LIVRD

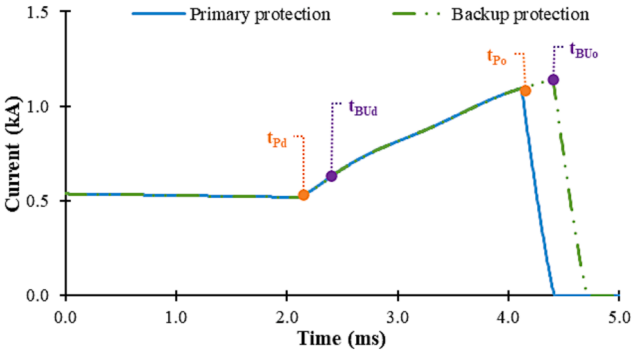

Fig. 13. Fault current measured by relay R14 for a 250 Ω PtG fault (F2) located in link 14.

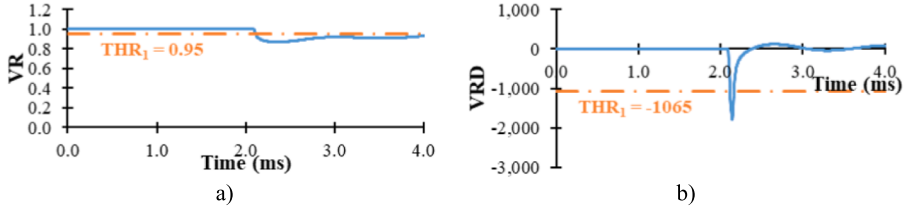

Fig. 11. a) VR and b) VRD signals measured by relay R14 for a 250 Ω PtG fault (F2) located in link 14.

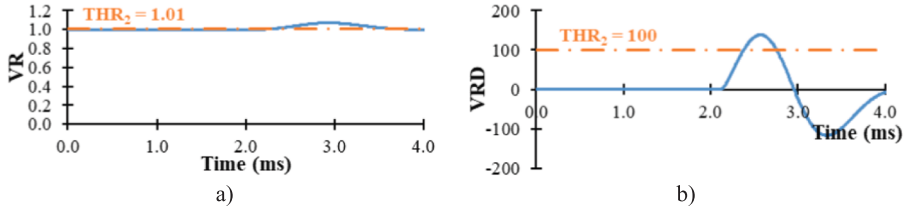

Fig. 12. a) VR and b) VRD signals measured by relay R12 for a 250 Ω PtG fault (F2) located in link 14.

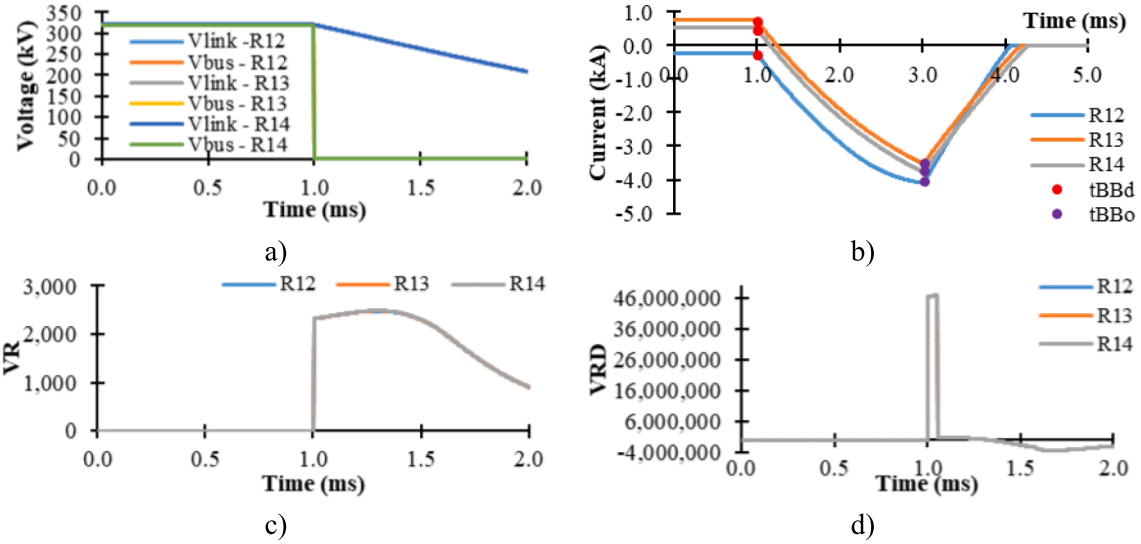

Fig. 14. Measurements taken by relays R12, R13 and R14 during a solid fault at Bus 1: a) Vlink and Vbus, b) fault currents, c) VR and d) VRD.

Table 2
Fault detection time (in ms) of the LIVRD protection scheme (forward fault detection).

	0 Ω	50 Ω	100 Ω	150 Ω	200 Ω	250 Ω
0 km	0.050	0.050	0.050	0.050	0.050	0.050
25 km	0.150	0.150	0.150	0.150	0.150	0.150
50 km	0.300	0.300	0.300	0.300	0.300	0.300
75 km	0.450	0.450	0.450	0.450	0.450	0.450
100 km	0.600	0.600	0.600	0.600	0.600	0.600
125 km	0.700	0.700	0.700	0.750	0.750	0.750
150 km	0.850	0.850	0.850	0.850	0.900	0.900
175 km	1.000	1.000	1.000	1.000	1.000	1.050
200 km	1.150	1.150	1.150	1.150	1.150	1.150

algorithm during different fault case scenarios varying the fault location and resistance is analysed. The simulated fault is located in link 14 while varying its resistance between 0 and 250 Ω and its location from relay R14 between 0 and 200 km. All the simulated scenarios are PtG faults since PtP faults are rare in cable-based systems. Table 2 summarizes the results of this analysis. The fault detection times are indicated in milliseconds from fault inception and correspond with relay R14.

As it can be seen in the table, the fault detection time of the LIVRD protection scheme is not significantly affected by the fault location and resistance. All simulated cases are detected right after the arrival of the fault-induced traveling wave to the relay point. Thus, the fast operation of the proposed LIVRD protection scheme is demonstrated.

3.6. *Influence of the noise disturbance*

All the analyses performed so far have supposed ideal measurements. However, in a real implementation the values measured have a noise component due to the non-ideal nature of the measurement devices. This way, the performance of the proposed protection scheme under noise disturbance conditions is analysed in this subsection.

A solid fault F3 (fault inception is at t = 1 ms) located in link 12, right in front of relay R12 is simulated for a range of signal-to-noise ratios of 30, 40 and 50 dB. The SNR is a parameter that compares the desired signal power to the background noise power, as in (21).

$$\mathrm{SNR} = 10 \cdot \log\left(\frac{P_{signal}}{P_{noise}}\right) \tag{21}$$

where P_{signal} is the power of the signal and P_{noise} is the power of the background noise.

Thus, a low SNR means a higher level of noise in relation to the

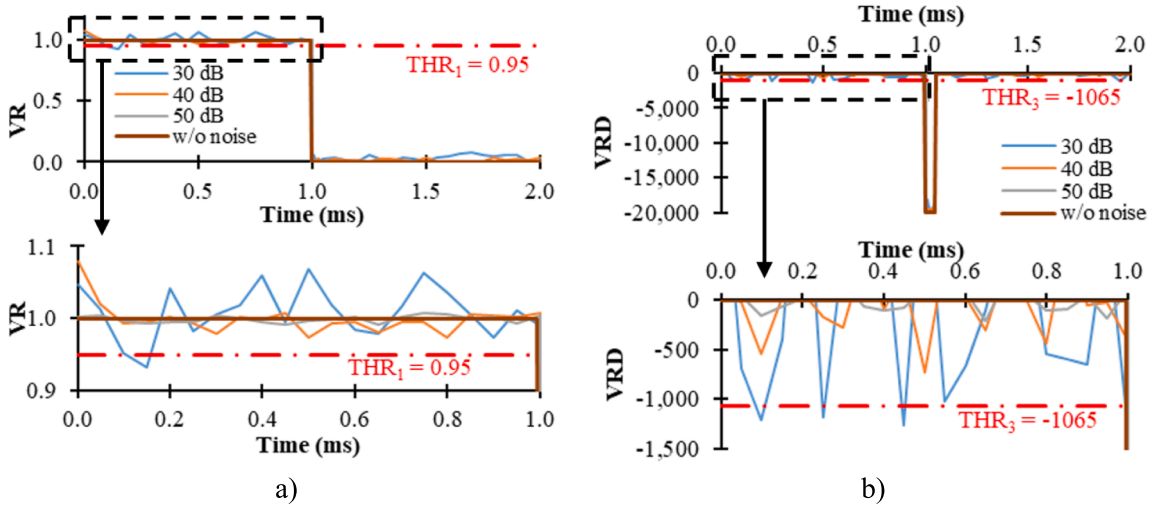

Fig. 15. a) VR and b) VRD signals measured by relay R12 for a solid PtG fault (F3) located in link 12 under noise disturbances.

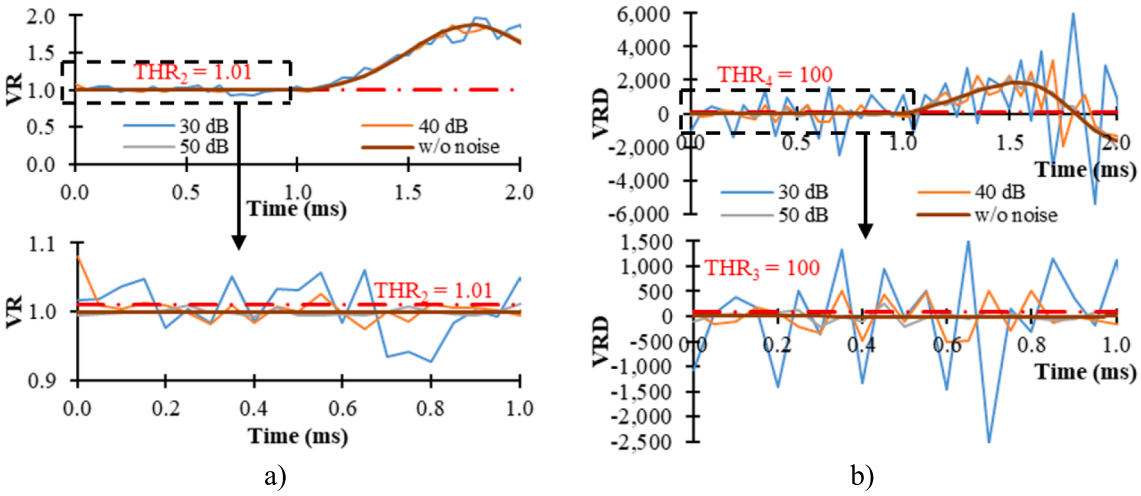

Fig. 16. a) VR and b) VRD signals measured by relay R13 for a solid PtG fault (F3) located in link 12 under noise disturbances.

signal. The range of SNRs employed in this subsection has been selected according to other similar analyses found in the literature [33].

The following figures show VR and VRD curves with SNR from 30 to 50 dB. Fig. 15 corresponds to relay R12 and Fig. 16 corresponds to relay R13. These figures also show additional graphics with zoom in the pre-fault regime of the simulations in order to present a better visualization of the influence of the noise disturbance.

As it can be seen, the VRD measurement is more impacted by the noise disturbance than the VR one since derivative calculations are more affected by the alterations in the ideal signal; these abrupt changes are easily detected by derivative calculations so it might produce a nuisance protection operation. Relay R12 is able to properly detect the fault under all the simulated fault cases with a SNR above 40 dB. During normal conditions, VR and VRD values do not satisfy the fault detection conditions while the fault is quickly detected after fault inception. However, a SNR of 30 dB causes the fulfilment of the fault detection criteria during normal operation conditions, thus, a nuisance operation might take place.

On the other hand, the VRD calculation of the link backup protection of relay R13 is significantly affected by the noise disturbance for a SNR of 30 and 40 dB and a nuisance operation might occur. However, the link backup protection properly operates for SNRs of 50 dB or higher.

According to this, the proposed link primary protection presents proper operation under noise disturbances over a SNR of 40 dB while link backup protection can encompass SNRs of 50 dB or higher.

3.7. Comparison with other algorithms

Finally, in this subsection, the LIVRD algorithm's features are compared with those of other inductor-voltage-based algorithms found in the literature.

Authors of [23] have made use of the voltage across the limiting inductors as the fault indicator. This parameter allows discrimination between forward and backward faults however its performance against high-resistance faults is limited to 50 Ω (0.22 pu, using as base, the rated power and voltage of the studied system).

Similarly, reference [24] uses the voltage across the limiting inductor for fault detection and fault type and faulty pole identification in an OHL-based system. Nevertheless, it uses a relatively large inductor size of 150 mH.

On the other hand, other researchers have analysed the difference between the ROCOV at both sides of the inductors with the purpose of discriminating between internal and external fault conditions [25,26]. This way, the ratio between the link-side ROCOV and the bus-side ROCOV is compared to a threshold value for fault detection. However, this protection scheme needs the supervision of an undervoltage element for its correct operation, which can limit its performance in terms of high-resistance fault detection and operation speed. Thus, the technique does not present a sensitive performance against high-resistance fault conditions, i.e., over 50 Ω for cables and over 200 Ω for overhead lines (0.12 and 0.49 pu, respectively, using as base, the rated power and voltage of the studied system [25,26]). Hence, the authors introduce a communication system between both ends of the protection zone [25] which reduces the operation speed of the protection system. In addition, they employ a relatively high sampling frequency for the voltage-derivative calculation, i.e., 32 kHz [25] and 25 kHz [26].

Reference [27] uses as fault marker the voltage across the terminal inductors of the converter. The voltage is monitored and compared to two threshold values. If the time taken by the voltage to cross both voltage threshold values is lower than a certain time interval, fault detection is achieved. It detects PtP faults up to 1000 Ω (1 pu, using as base the rated power and voltage of the studied system). However, PtG faults are not considered in the study, even though, they are more common than PtP faults. Moreover, it uses 200 mH inductors.

Conversely, the LIVRD algorithm presents the lowest sampling frequency (20 kHz) and a relatively low inductor size of 100 mH, while presenting high sensitivity to high-resistance faults, up to 250 Ω for both PtG and PtP faults in a cable-based meshed grid (0.73 pu, using as base, the rated power and voltage of 1200 MVA and 320 kV). Besides, it is a single-ended algorithm which does not employ communication channels in its performance, so fast operation is ensured. Moreover, it is able to detect and properly discriminate between internal and external faults, enabling primary and backup protection. Fault detection time is not affected by the fault resistance and it could be adapted to detection of higher fault resistances by selecting new threshold values since those employed in the study case were selected taking into account a maximum fault resistance of 250 Ω. Additionally, the influence of the noise disturbance on its operation has been analysed and it presents a robust operation for SNR values of 40 dB or higher (50 dB for backup protection). Thus, it can be said that the proposed LIVRD presents great features since it overcomes the sensitivity limitations related to derivative-based algorithms while employing low sampling frequency and inductor size.

The main characteristics of the abovementioned algorithms are summarized in Table 3. In this table, it is noticeable that the features of the proposed LIVRD algorithm exceed those of the remaining algorithms.

Table 3
Comparison of inductor-voltage-based algorithms.

Algorithm	Communication channel	Noise disturbance	Inductor size	Sampling frequency	Fault resistance
[23]	No	Not analysed	30 mH	Not applicable	PtG, PtP – 50 Ω (0.22 pu; cable)
[24]	Yes	Not analysed	150 mH	Not applicable	PtG – 380 Ω (0.76 pu; OHL) PtP – 600 Ω (1.2 pu; OHL)
[25]	Yes	Not analysed	50, 100, 150 mH	32 kHz	PtG – 50 Ω (0.12 pu; cable) PtG – 200 Ω (0.49 pu; OHL) PtP – Not considered
[26]	No	Not analysed	40 mH	25 kHz	PtG – 50 Ω (0.12 pu; cable) PtP – Not considered (cable) PtP – 200 Ω (0.49 pu; OHL)
[27]	No	Not analysed	100, 200 mH	Not applicable	PtP – 1000 Ω (1 pu; cable) PtG – Not considered
LIVRD	No	SNR $\geq$ 40 dB (link primary prot.) SNR $\geq$ 50 dB (link backup prot.)	100 mH	20 kHz	PtP, PtG – 250 Ω (0.73 pu; cable)

4. Conclusions

Single-ended protection systems have been widely studied in the last years for their application to HVDC grids due to their advantageous operation speed. According to this tendency, this work proposes a protection algorithm consisting in the voltage-ratio between the voltage measurements taken at both sides of the limiting inductor and its derivative. This protection algorithm presents a directionality capability provided by the voltage-ratio and a fast operation speed due to the calculation of the voltage-ratio-derivative. This way, the combination of these two algorithms provide selective operation and discrimination between forward and backward faults. Fault detection is only achieved when their individual criteria are simultaneously fulfilled.

Taking into account the fault discrimination capability between forward and backward faults presented in the LIVRD algorithm, a protection scheme is developed. It covers the link primary and backup protections as well as the busbar protection. Its performance has been validated through simulations in PSCAD against different fault case scenarios, including the worst fault case scenarios. Its fault detection speed has also been assessed; it is not significantly affected by the fault resistance or the fault location. Similarly, the influence of the noise disturbance on its operation has also been evaluated. The link primary and backup protections can properly operate for SNRs above 40 dB and 50 dB, respectively, which are values similar to those found in the literature.

Moreover, the proposed LIVRD algorithm has been compared with other similar algorithms and it can be concluded that it can overcome the sensitivity limitations related to detection of high-resistance faults while employing only locally available measurements and relatively low sampling frequencies and common inductor sizes of 20 kHz and 100 mH, respectively. It has been demonstrated that the proposed protection scheme presents fast, selective and sensitive operation under different fault case scenarios including noise disturbances.

Funding

The authors gratefully acknowledge the support from the Basque Government (GISEL research group IT1522-22) and the University of the Basque Country UPV/EHU (PIF 20/06).

CRediT authorship contribution statement

María José Pérez-Molina: Conceptualization, Methodology, Software, Validation, Formal analysis, Investigation, Data curation, Writing – original draft, Writing – review & editing, Visualization, Project administration, Funding acquisition. **Pablo Eguia:** Conceptualization, Methodology, Resources, Writing – review & editing, Visualization, Supervision, Funding acquisition. **D. Marene Larruskain:** Conceptualization, Methodology, Resources, Writing – original draft, Writing – review & editing, Visualization, Supervision, Funding acquisition. **Esther Torres:** Conceptualization, Methodology, Resources, Writing – review & editing, Visualization, Supervision. **Oihane Abarrategi:** Conceptualization, Methodology, Resources, Writing – review & editing, Visualization, Supervision. **Juan C. Sarmiento-Vintimilla:** Conceptualization, Methodology, Writing – review & editing, Visualization.

Declaration of Competing Interest

The authors declare that they have no known competing financial interests or personal relationships that could have appeared to influence the work reported in this paper.

Data availability

Data will be made available on request.

References

[1] Arita Torres J, dos Santos RC, Yang Q, Li J. Analyses of different approaches for detecting, classifying and locating faults in a three-terminal VSC-HVDC system. Int J Electr Power Energy Syst 2022;135:107514.
[2] Xiang W, Yang S, Adam GP, Zhang H, Zuo W, Wen J. DC Fault Protection Algorithms of MMC-HVDC Grids: Fault Analysis, Methodologies, Experimental Validations, and Future Trends. IEEE Trans Power Electron 2021;36(10):11245–64.
[3] Mohammadi F, Rouzbehi K, Hajian M, Niayesh K, Gharehpetian GB, Saad H, et al. HVDC Circuit Breakers: A Comprehensive Review. IEEE Trans Power Electron 2021:1.
[4] Tu Y, Pei X, Zhou W, Li P, Wei X, Tang G. An integrated multi-port hybrid DC circuit breaker for VSC-based DC grids. Int J Electr Power Energy Syst 2022;142:108379.
[5] Li R, Xu L. Review of DC fault protection for HVDC grids. WIREs Energy and Environment, vol. 7, (2), 2018.
[6] Shu H, Wang G, Tian X, Ju X, An N, Bo Z. MMC-HVDC line fault identification scheme based on single-ended transient voltage information entropy. Int J Electr Power Energy Syst 2022;141:107817.
[7] Buigues G, Valverde V, Zamora I, Larruskain DM, Abarrategui O, Iturregi A. DC fault detection in VSC-based HVDC grids used for the integration of renewable energies", in 2015 International Conference on Clean Electrical Power (ICCEP), Taormina, Italy, 16-18 June 2015, pp. 666-673.
[8] Wang Y, Yuan Z, Fu J, Li Y, Zhao Y. A feasible coordination protection strategy for MMC-MTDC systems under DC faults. Int J Electr Power Energy Syst 2017;90:103–11.
[9] Jahn I, Johannesson N, Norrga S. Survey of methods for selective DC fault detection in MTDC grids. In: 13th IET International Conference on AC and DC Power Transmission (ACDC 2017), Manchester, UK, 14-16 February 2017.
[10] Pérez Molina MJ, Larruskain DM, Eguía López P, Etxegarai A. Analysis of Local Measurement-Based Algorithms for Fault Detection in a Multi-Terminal HVDC Grid. Energies 2019;12:(24).
[11] Ikhide MA, Tennakoon SB, Griffiths A, Subramanian S, Ha H, Adamczyk A. Limitations of di/dt technique in DC line protection. In: 13th International Conference on Development in Power System Protection 2016 (DPSP), Edinburgh, UK, 7-10 March 2016.
[12] Sneath J, Rajapakse AD. DC fault protection of a nine-terminal MMC HVDC grid. In: 11th IET International Conference on AC and DC Power Transmission, Birmingham, UK, 10-12 February 2015.
[13] Geddada N, Yeap YM, Ukil A. Experimental Validation of Fault Identification in VSC-Based DC Grid System. IEEE Trans Ind Electron 2018;65(6):4799–809.

[14] Sneath J, Rajapakse AD. Fault Detection and Interruption in an Earthed HVDC Grid Using ROCOV and Hybrid DC Breakers. IEEE Trans Power Delivery 2016;31(3):973–81.
[15] Zou G, Feng Q, Huang Q, Sun C, Gao H. A fast protection scheme for VSC based multi-terminal DC grid. Int J Electr Power Energy Syst 2018;98:307–14.
[16] Torres J, Santos R, Asano P. A comparison of new methods based on ANNs for detecting and locating faults in MTDC systems. In: 2018 International Conference on Smart Energy Systems and Technologies (SEST), Sevilla, Spain, 10-12 September 2018.
[17] Psaras V, Emhemed A, Adam G, Burt GM. Review and evaluation of the state of the art of DC fault detection for HVDC grids. In: 2018 53rd International Universities Power Engineering Conference (UPEC), Glasgow, Scotland, 4-7 September 2018.
[18] Pérez-Molina MJ, Larruskain DM, Eguia P, Valverde V. Local derivative-based fault detection for HVDC grids. IEEE Trans Ind Appl 2022;58(2):1521–30.
[19] Pérez-Molina MJ, Larruskain DM, Eguía López P, Buigues G. "Challenges for Protection of Future HVDC Grids", Frontiers in Energy Research, vol. 8, 2020.
[20] Perez-Molina MJ, Larruskain DM, Eguia Lopez P, Buigues G, Valverde V. Review of protection systems for multi-terminal high voltage direct current grids. Renew Sustain Energy Rev, vol. 144, 2021.
[21] Yang C, Xin Y, Li C, Li Q, Yang T, Lu J, et al. Fault protection of multiterminal HVDC networks: Impact of inductance. Int J Electr Power Energy Syst 2022;141:108113.
[22] Hajian M, Jovcic D, Wu B. Evaluation of Semiconductor Based Methods for Fault Isolation on High Voltage DC Grids. IEEE Trans Smart Grid 2013;4(2):1171–9.
[23] Descloux J, Raison B, Curis J. Protection algorithm based on differential voltage measurement for MTDC grids. In: 12th IET International Conference on Developments in Power System Protection (DPSP 2014), Copenhagen, Denmark, 31 March-3 April 2014.
[24] Li C, Gole AM, Zhao C. A Fast DC Fault Detection Method Using DC Reactor Voltages in HVdc Grids. IEEE Trans Power Delivery 2018;33(5):2254–64.
[25] Haleem NM, Rajapakse AD. Application of new directional logic to improve DC side fault discrimination for high resistance faults in HVDC grids. J Mod Power Syst Clean Energy 2017;5(4):560–73.
[26] Haleem NM, Rajapakse AD. Local measurement based ultra-fast directional ROCOV scheme for protecting Bi-pole HVDC grids with a metallic return conductor. Int J Electr Power Energy Syst 2018;98:323–30.
[27] Li R, Xu L, Yao L. DC Fault Detection and Location in Meshed Multiterminal HVDC Systems Based on DC Reactor Voltage Change Rate. IEEE Trans Power Delivery 2017;32(3):1516–26.
[28] Yang S, Xiang W, Li R, Lu X, Zuo W, Wen J. An Improved DC Fault Protection Algorithm for MMC HVDC Grids Based on Modal-Domain Analysis. IEEE J Emerg Selec Top Power Electron 2020;8(4):4086–99.
[29] Huai Q, Qin L, Liu K, Hooshyar A, Ding H, Gong C, et al. A pilot line protection for MT-HVDC grids using similarity of traveling waveforms. Int J Electr Power Energy Syst 2021;131:107162.
[30] Leterme W, Ahmed N, Beerten J, Ängquist L, Hertem DV, Norrga S. A new HVDC grid test system for HVDC grid dynamics and protection studies in EMT-type software. In: 11th IET International Conference on AC and DC Power Transmission, Birmingham, UK, 10-12 February 2015.
[31] Leterme W, Ahmed N, Beerten J, Ängquist L, Van Hertem D, Norrga S. (29/10/2015) HVDC grid test system for EMT studies. Available: https://www.esat.kuleuven.be/electa/hvdcresearch/hvdc-test-grid (Accessed on 22 March 2022).
[32] Descloux J, Gandioli C, Raison B, Hadjsaid N, Tixador P. Protection system for meshed HVDC network using superconducting fault current limiters. In: 2013 IEEE Grenoble Conference, Grenoble, France, 16-20 June 2013.
[33] Jiang L, Chen Q, Huang W, Wang L, Zeng Y, Zhao P. "Pilot Protection Based on Amplitude of Directional Travelling Wave for Voltage Source Converter-High Voltage Direct Current (VSC-HVDC). Transmission Lines", Energies 2018;11:(8).